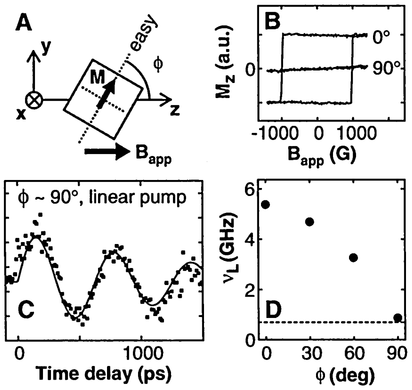

Fig. 5. (**A**) Schematic drawing: the MnAs sample is rotated in-plane to create an angle ϕ between the easy axis and the applied field. (**B**) MOKE hysteresis loops taken with magnetic field applied along the easy axis ($\phi = 0°$) and the hard axis ($\phi = 90°$) of the MnAs sample. The hard axis loop shows a negligible magnetization component along the applied field, indicating that the magnetization direction remains very close to the easy axis even in the presence of a non-collinear applied field. (**C**) Linearly pumped TRFR time scan at 5 K with $\phi \sim 90°$ and $B_{app} = 1000$ G. The pump intensity is ~100 W/cm^2. The presence of spin-precession indicates that the ferromagnet polarizes some fraction of the photoexcited electrons along the magnetization. The solid line is a guide to the eye. (**D**) The Larmor frequency at 5 K, 1000 G for different angles ϕ, measured by standard (circularly pumped) TRFR. The dashed line represents the spin precession due to the applied field (Zeeman), and the additional frequency is a measure of the nuclear polarization.

angle $\phi \sim 90°$ causes the magnetization to orient perpendicular to the applied field, while maintaining the normal incidence of the pump beam. In this sample geometry, a linearly polarized pump pulse is used in place of the circularly polarized pump pulse in the TRFR measurement so that the optical excitation imparts no angular momentum to the sample. However, a time scan with B_{app} = 1000 G exhibits precession of coherent electron spins (Fig. 5C) (*27*), indicating that these electrons acquire a component of spin-polarization perpendicular to the field (i.e., along the magnetization). Because this angular momentum does not originate from the pump pulse, it demonstrates that the ferromagnet polarizes some fraction of the photoexcited electrons along the magnetization. Currently, it is unclear how the ferromagnet polarizes the photoexcited electrons; some possibilities include polarization during the absorption process, spin-dependent recombination with spin-polarized holes, and spin-dependent scattering at the ferromagnetic interface. Nonetheless, this result implies that photoexcited electrons mediate the transfer of angular momentum from the ferromagnet to the nuclear spins in GaAs.

Finally, we show that the nuclear polarization depends primarily on the component of magnetization parallel to the applied field. The angle ϕ between the magnetization **M** and $\mathbf{B}_{app}$ is varied systematically by rotating the sample in-plane (Fig. 5A). Returning to TRFR measurement with a circularly polarized pump pulse, ν_L is measured for several angles ϕ (Fig. 5D), and the nuclear polarization corresponds to ν_L in excess of the Zeeman contribution (dashed line). As the parallel component of magnetization vanishes at $\phi = 90°$, the nuclear polarization also approaches zero. This behavior is explained by considering the components of electron spin involved in DNP. The circularly polarized pump induces electron spin S_x normal to the sample (axes defined in Fig. 5A). The ferromagnet induces in-plane spin-polarization both parallel to the field $S_z \sim M_z \sim \cos\phi$ and perpendicular to the field $S_y \sim M_y \sim \sin\phi$. DNP depends primarily on the projection of the total electron spin on $\mathbf{B}_{app}$ (i.e., S_z) (*9*), explaining why M_z is the most important component for generating nuclear polarization.

References and Notes

1. M. N. Baibich *et al.*, *Phys. Rev. Lett.* **61**, 2472 (1988).
2. J. M. Kikkawa, D. D. Awschalom, *Phys. Rev. Lett.* **80**, 4313 (1998).
3. M. Tanaka *et al.*, *Appl. Phys. Lett.* **65**, 1964 (1994).
4. H. Ohno, *Science* **281**, 951 (1998).
5. Y. Ohno *et al.*, *Nature* **402**, 790 (1999).
6. R. K. Kawakami *et al.*, *Appl. Phys. Lett.* **77**, 2379 (2000).
7. H. Ohno *et al.*, *Nature* **408**, 944 (2000).
8. D. P. DiVincenzo, *J. Appl. Phys.* **85**, 4785 (1999); D. Loss, D. P. DiVincenzo, *Phys. Rev. A* **57**, 120 (1988).
9. F. Meier, B. P. Zakharchenya, Eds., *Optical Orientation* (North-Holland, New York, 1984).
10. J. M. Kikkawa, D. D. Awschalom, *Science* **287**, 473 (2000).
11. G. Salis *et al.*, *Phys. Rev. Lett.* **86**, 2677 (2001).
12. S. A. Crooker, J. J. Baumberg, F. Flack, N. Samarth, D. D. Awschalom, *Phys. Rev. Lett.* **77**, 2814 (1996).
13. Growth conditions for ferromagnetic layers: T_{growth} = 240°C (MnAs) or 260°C [(Ga,Mn)As, DFH, single layer]; As$_4$/Ga flux ratio ~25; GaAs rate ~5 nm/min; MnAs rate ~0.3 nm/min.
14. H. Tanobe, F. Koyama, K. Iga, *Jpn. J. Appl. Phys.* **31**, 1597 (1992).
15. The *n*-GaAs control sample has $g = -0.50$.
16. Supplemental figure is available at www.sciencemag.org/cgi/content/full/294/5540/131/DC1.
17. This evolution of ν_L includes a zero-crossing at ~2 min after reversal, which indicates that ν_L changes sign (i.e., spin precession changes direction) in response to a magnetization reversal.
18. Therefore, the exact shape of the ν_L curves in Fig. 2 depends on the field step and acquisition rate.
19. As ν_L approaches zero, its value cannot be resolved below 0.1 GHz due to the limited range of Δt (0 to 2600 ps) accessible by the delay line.
20. D. Paget, G. Lampel, B. Sapoval, V. I. Safarov, *Phys. Rev. B* **15**, 5780 (1977).
21. D. Gammon *et al.*, *Phys. Rev. Lett.* **86**, 5176 (2001).
22. V. K. Kalevich, *Sov. Phys. Solid State* **28**, 1947 (1986).
23. D. R. Lide, Ed., *CRC Handbook of Chemistry and Physics* (CRC Press, Boca Raton, FL, 1993).
24. A. W. Overhauser, *Phys. Rev.* **92**, 411 (1953).
25. G. Lampel, *Phys. Rev. Lett.* **20**, 491 (1968).
26. K. Bärner, R. Braunstein, E. Chock, *Phys. Status Solidi B* **80**, 451 (1977).
27. R. J. Epstein, *et al.*, in preparation.
28. We would like to thank J. English for technical assistance and acknowledge support from Defense Advanced Research Projects Agency, the Office of Naval Research, the Air Force Office of Scientific Research, and NSF.

6 June 2001; accepted 20 August 2001

Spatiotemporal Addressing of Surface Activity

Janpeter Wolff,[1] Athanasios G. Papathanasiou,[1]
Ioannis G. Kevrekidis,[2*]
Harm Hinrich Rotermund,[1,2] Gerhard Ertl[1]

We have modified surface catalytic activity in real time and space by focusing an addressable laser beam to differentially heat a platinum (110) single-crystal surface. Ellipsomicroscopy imaging of local conditions (such as reactant and product local coverages) enabled us to close the loop between sensing and actuation (both spatiotemporally resolved). Pulses and fronts, the basic building blocks of patterns, could be formed, accelerated, modified, guided, and destroyed at will. Real-time image processing and feedback allow the design and implementation of new classes of nonlocal evolution rules.

The interaction of reaction and transport can lead to pattern formation in reacting systems. Influencing the spatiotemporal pathway of chemical reactions is an active area of research in many branches of science and engineering, from cell biology (*1*) to industrial reactor design (*2*). Overall behavior can be altered by changing the system size (*3–5*), by forcing through an external periodic perturbation (*6*), or simply by feedback (*7, 8*). We have now connected spatially distributed sensing with locally resolved actuation to form a spatiotemporally addressable catalytic medium for CO oxidation.

During the last decade, pattern formation for several catalytic reactions (such as CO + O$_2$, NO + CO, NO + H$_2$, and H$_2$ + O$_2$) has been studied over wide ranges of operating condi-

---

[1] Fritz-Haber-Institut der Max-Planck-Gesellschaft, Faradayweg 4-6, 14195 Berlin, Germany. [2] Department of Chemical Engineering, Princeton University, Princeton, NJ 08544, USA.

*To whom correspondence should be addressed. E-mail: yannis@princeton.edu

tions (temperature and reactant partial pressures) on single-crystal and polycrystalline Pt, Pd, and Rh surfaces. These studies, made possible through the substantial improvement of space-time–resolving techniques (*9*), confirmed the reaction-diffusion basis of catalytic patterns ranging from spiral waves to chemical turbulence (*10–12*). The interaction of a multitude of micrometer-scale concentration waves and fronts on the surface complicate understanding and elucidating the underlying mechanisms for such patterns. Experiments have therefore been designed to isolate individual features (e.g., single pulses) and interaction mechanisms in order to study them quantitatively (*13*). This concept is illustrated in Fig. 1A, where a target pattern for CO oxidation on Pt(110) is isolated in a complex geometric structure. Figure 1B displays a multitude of spirals on a surface with a submonolayer of Ti deposited on it, leaving an H-shaped Pt area uncovered. Varying the geometry (size, shape, and even height) of these catalytic domains constitutes, in effect, a means of influencing the spontaneous spatial scales of the patterns. A natural next step is the construction of microcomposite catalysts, where the boundaries of the reacting regions are not inert, but consist of a different, also catalytically active, medium. In this case, we try to affect the chemistry itself through the choice of the second active medium and its distribution in space. Figure 1C demonstrates that regular grids of active Rh inclusions generate wavefronts on Pt when an open Pt surface cannot sustain them. This change in local reactivity due to microdesigned heterogeneities has now been studied for several catalyst combinations (*3*, *14–17*)

One can also interact with the temporal scales of reaction and transport processes. Applying global, uniform in space, temporally periodic forcing, researchers have pursued improvements in overall reactor performance (*18*, *19*). By analogy, the geometry of a composite catalyst constitutes spatially varying—but temporally constant—forcing of the catalytic reaction. Various types of spatiotemporal forcing have led recently to the discovery of new types of reactive patterns (*6*, *20*, *21*).

Temporal feedback provides an additional dimension in our ability to interact with spontaneous pattern formation. A typical systems theory objective of feedback would be the stabilization of an unstable state, or the tracking of an external set point (*22*, *23*). Novel objectives (such as the exploration of the role of global time-delayed feedback) are also being actively pursued (*8*, *24–27*). The suppression of chemical turbulence and creation of novel intermittent as well as cluster patterns have been reported recently (*8*).

We have now controlled the local activity of a catalytic surface in both real time and space with an addressable focused laser beam that changes local conditions by differentially heating the catalyst. The location and size of the heating spot and the power delivered are computer controlled in real time, and can interact with the patterns over a wide range of space and time scales. Real-time imaging of the system state (the resulting patterns), coupled with real-time image processing and closing the loop through feedback, enables us to interact with catalytic pattern formation in new ways.

We demonstrate the use of this hybrid "experiment-software" system in two modes. First, we show that we can form, destroy, accelerate, modify, and guide at will basic building blocks of spontaneous patterns (pulses and fronts) on the surface. Some of these objectives are attained in open loop, through spatially distributed forcing; the experimenter or the computer or both can close the loop (*28*). Some of these tasks have been accomplished before in homogeneous catalytic systems (*20*, *29*, *30*). Second, we demonstrate the implementation, through distributed sensing and feedback, of what one might term "arbitrary evolution rules"—nonlocal interaction mechanisms on the surface that go beyond the nature of adsorption, desorption, surface diffusion, and reaction.

We imaged a Pt(110) surface (*31*), using ellipsomicroscopy for surface imaging (EMSI) (*32*), a recently developed method that is operable at any desired pressure. Here we added a 488-nm interference filter in front of the charge-coupled device camera to prevent most of the scattered light created by the heating laser from reaching the imaging camera.

The laser used for local heating was a multimode, continuous-wave Ar-ion laser with a maximum power of 7 W and focused to about 80 μm in diameter at the sample. At this power one can raise the crystal temperature a maximum of 110 K above room temperature (*33*). The spot can be moved within 1 ms to any point on the surface of our viewing field (~2 mm by 1 mm) with a spatial precision of 5 μm by using a pair of computer-controlled galvanometer mirrors (GSI Lumonics, M3ST). Because we used a multiline laser for maximizing local heating power, EMSI always showed some scattered light from the laser spot helping to guide it along the surface, as it still can be seen in the images presented below.

We first demonstrate the creation of wave fronts in an excitable regime (Fig. 2A). The four images display the response of the system to a slow, steady movement of the heating spot along a straight line across the surface. After the surface was completely covered with CO by establishing a fixed partial pressure of CO, the O_2 partial pressure was suddenly increased to a predetermined setting. The stationary heating spot locally desorbed CO from the surface and created target patterns, as can be seen at the left-hand side of Fig. 2A, consistent with the excitable nature of the medium. Once the first elliptical oxygen pulses formed, dragging the spot across the surface with constant velocity, we created a V-shaped pulse, reminiscent of a Mach cone, a form of wave front not observed under standard reaction diffusion conditions. Increasing the speed of the laser movement decreased the angle of the cone until, at a specific critical dragging speed, the front would no longer stay attached to the laser spot. In this case, our actuator is a single moving "pixel" in the resolution available. Short movies for Figs. 2 and 3 can be found at our Web site (http://w3.rz-berlin.mpg.de/~rotermun/science).

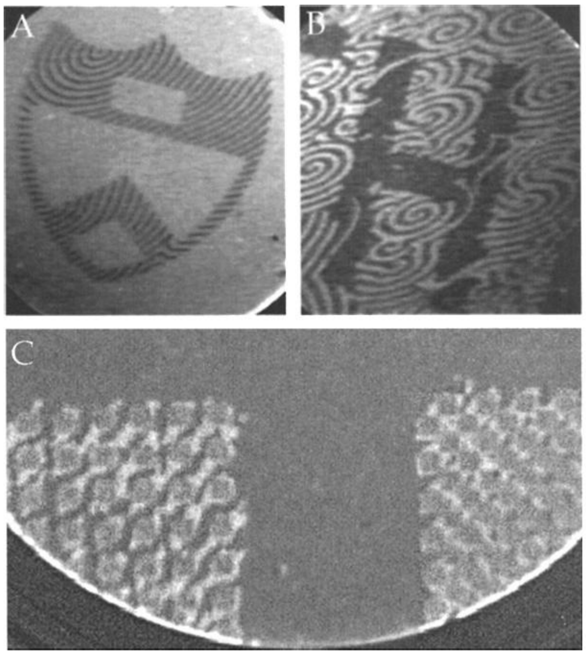

Fig. 1. (**A**) Pattern formation during CO oxidation in microdesigned catalytic domains. The clean Pt surface is in the shape of the Princeton "shield" (height, 350 μm). The surrounding surface is covered by 2000 Å thick inert Ti. Experimental conditions: $p_{O_2} = 4 \times 10^{-4}$ mbar, $p_{CO} = 3.6 \times 10^{-5}$ mbar, $T = 434$ K [see also (*37*)]. (**B**) The height of the letter H (clean Pt surface) is 350 μm ($p_{O_2} = 4 \times 10^{-4}$ mbar, $p_{CO} = 5.5 \times 10^{-5}$ mbar, $T = 440$ K). (**C**) The dark area is the clean Pt(110) surface covered by oxygen. Two patches are visible in which a grid of Rh squares of 100 μm² are deposited on the Pt. Around these patches an enhanced CO adsorption (bright areas) can be seen ($p_{O_2} = 4 \times 10^{-4}$ mbar, $p_{CO} = 1.3 \times 10^{-4}$ mbar, $T = 524$ K).

Closing of the feedback loop by the experimenter is shown in Fig. 2B, in which a multitude of CO fronts travel around the surface. The experimenter directed the laser spot at a moving front by tracking it with a computer mouse, heating and thereby erasing it. Figure 2B shows four stages in the annihilation of a rather irregular CO front; the time required is indicative of the speed of the operator's physiological response.

A different objective is illustrated in Fig. 2C. The laser produced a corridor, in this case an annulus defined by boundaries of higher temperature. Two concentric circles of circumferences 1.6 and 3.5 mm were drawn every 1.5 s. The heating protocol started with the unperturbed surface in the excitable regime, and when the first "heat walls" were raised, a CO pulse was trapped between them. The sequence of six images in Fig. 2C depicts the trajectory of this pulse, indicated by the arrow in the first frame. The pulse moves downward, curls around to the left, and starts to form a spiral when the corridor aligns with the fast diffusion direction on the anisotropic crystal. The temperature walls of this corridor, which are continuously being refreshed by the circulating laser, can be contrasted with the material corridors in Fig. 1B. As the pulse continues clockwise, it curls again when it encounters the fast diffusion direction and returns to its original shape. These heat walls control the pulse movement along a (periodic) path that it would not have taken itself; writing arbitrary hot corridors can deliver the CO pulse to any desired location on the surface.

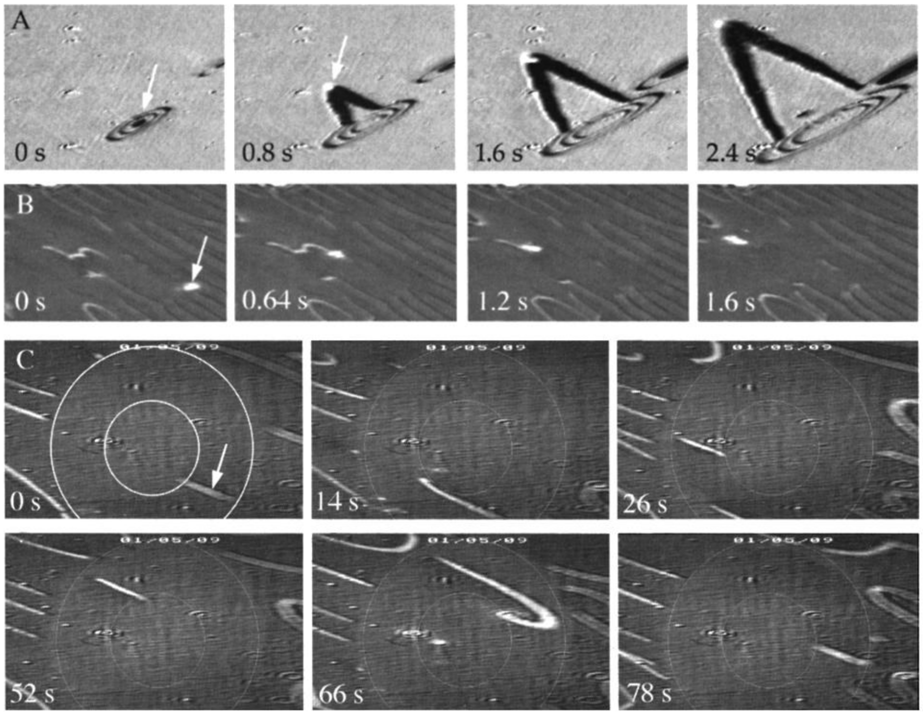

Fig. 2. (**A**) $p_{O_2} = 3 \times 10^{-4}$ mbar, $p_{CO} = 9 \times 10^{-5}$ mbar, $T = 515$ K. (**B**) $p_{O_2} = 3 \times 10^{-4}$ mbar, $p_{CO} = 7 \times 10^{-5}$mbar, $T = 505$ K. The images in (A) and (B) show an area of 1.5 mm by 1.1 mm and 1.0 mm by 0.6 mm, respectively. The arrows indicate the position of the laser spot. (**C**) The white circles with diameters 1.1 mm and 0.5 mm (thicker in the first image) denote the path the laser spot follows on the surface ($p_{O_2} = 3 \times 10^{-4}$ mbar, $p_{CO} = 5.1 \times 10^{-5}$ mbar, $T = 479$ K).

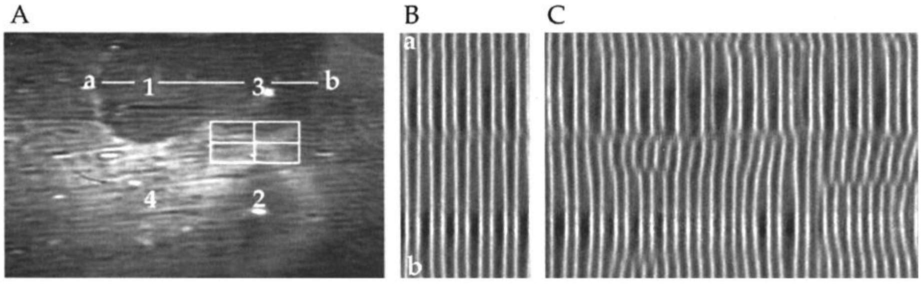

Fig. 3. (**A**) EMSI image showing the location of the four laser spots (1 to 4) and the line along which the space-time plots of (B) and (C) were taken (a-b, 750 μm). (**B**) Space-time plot (10 s) without feedback ($z = 0$). (**C**) Space-time plot (29 s) with feedback ($z = 0.9$). The feedback had been turned on 8 s earlier ($p_{O_2} = 3 \times 10^{-4}$ mbar, $p_{CO} = 7.5 \times 10^{-5}$ mbar, $T = 545$ K, $T_0 = 750$ ms).

In Fig. 3, the initial condition consisted of global homogeneous oscillations. The laser spot jumped between four points indicated by numbers 1, 2, 3, and 4 in Fig. 3A. The residence time at each spot i was $T_i = T_0/4$ (T_0 being the period of one heating cycle). Our particular (and, admittedly, rather arbitrary) feedback law was designed to demonstrate the flexibility and scope of the setup in addressing the experimental dynamics. It embodied (i) spatially distributed sensing (gray-scale image acquisition); (ii) real-time image processing (here, computing weighted local grayscale intensities); and (iii) distributed (possibly nonlocal and/or delayed) feedback (here, feedback based on both local and remote measurements). The feedback loop was thus built of several steps: First, the state of the surface was imaged. The image was processed and the averages (a_i) in the four arbitrarily chosen, rectangular regions, indicated by white lines in Fig. 3A, were computed. These four quantities were compared with their average ($\bar{a}$) and the heating times for the next cycle, T_i ($i = 1, 2, 3, 4$), were computed as follows:

$$T_i = \frac{T_0}{4\bar{a}} \left(z\,(a_j - \bar{a}) + (1 - z)\,\bar{a}\right)$$

In this equation, z defines the feedback strength (between 0 and 1). The assignment of the heating duration of a point i to measurements in a specific observation region j was decided randomly at the beginning of the experiment. Here we chose the gray-scale average of region 2 to determine T_1, and for the remaining pairing we decided on 4→2, 1→3, and 3→4, respectively. Figure 3A depicts a homogeneously oscillating base state perturbed by the four laser locations (heating for 185 ms at each spot). The resulting pattern was strictly periodic, as can be seen through the space-time diagram in Fig. 3B, which displays the temporal evolution of the pattern in the cross section along the line a-b in Fig. 3A. By closing the feedback loop, the pattern became irregular, illustrated in the corresponding space-time plot in Fig. 3C. Such a pattern probably could not be realized in open-loop CO oxidation.

Our aim here is to demonstrate the vast freedom, over ranges of space and time unprecedented in catalytic reactions, that this approach allows in addressing spatiotemporal pattern formation. Exploring the types of behavior accessible to such "arbitrary rule" closed-loop systems, combining physics and software to influence and control the behavior, is an open-ended task that requires direction and goals. Typical systems theory goals go beyond stabilization of unstable patterns and/or tracking desired setpoint behavior, to the study of robustness and the effects of noise, and more specifically, optimization of the system outputs. In our case this would suggest the design of spatiotemporal feedback laws to optimize average performance of the catalyst, including selectivity for the case of more complex catalytic pathways. Figure 2B suggests the local regeneration of deactivated areas as one possible starting point for such a design. In the case of island-forming reactants, for which the reaction occurs at the perimeter of these islands (*34*, *35*), the generation of additional boundaries should enhance reaction rates. What are good feedback laws for these objectives, and how can they be implemented? Hierarchical control schemes (*36*) may be key to the practical implementation of real-time feedback with finely distributed actuation.

References and Notes

1. J. A. Lundqvist *et al.*, *Proc. Natl. Acad. Sci. U.S.A.* **95**, 10356 (1998).
2. Y. S. Matros, G. A. Bunimovich, *Catal. Rev.-Sci. Eng.* **38**, 1 (1996).
3. M. X. Yang, D. H. Gracias, P. W. Jacobs, G. A. Somorjai, *Langmuir* **14**, 1458 (1998).
4. K. Wong, S. Johansson, B. Kasemo, *Faraday Discuss.*, **105**, 237 (1996).
5. R. Srinivasan *et al.*, *AIChE J.* **43**, 3059 (1997).
6. A. L. Lin *et al.*, *Phys. Rev. Lett.* **84**, 4240 (2000).
7. V. Petrov, V. Gaspar, J. Masere, K. Showalter, *Nature* **361**, 240 (1993).
8. M. Kim *et al.*, *Science* **292**, 1357 (2001).
9. H. H. Rotermund, *Surf. Sci. Rep.* **29**, 265 (1997).
10. ———, W. Engel, M. Kordesch, G. Ertl, *Nature* **343**, 355 (1990).
11. S. Jakubith, H. H. Rotermund, W. Engel, A. v. Oertzen, G. Ertl, *Phys. Rev. Lett.* **65**, 3013 (1990).
12. F. Mertens, R. Imbihl, *Nature* **370**, 124 (1994).
13. M. D. Graham *et al.*, *Science* **264**, 80 (1994).
14. J. Lauterbach *et al.*, *Physica D* **123**, 493 (1998).
15. S. Y. Shvartsman, E. Schütz, R. Imbihl, I. G. Kevrekidis, *Phys. Rev. Lett.* **83**, 2857 (1999).
16. M. Kolodziejczyk, R. E. R. Colen, B. Delmon, J. H. Block, *Appl. Surf. Sci.* **121**, 480 (1997).
17. F. Esch *et al.*, *Catal. Lett.* **52**, 85 (1998).
18. Y. S. Matros, *Can. J. Chem. Eng.* **74**, 566 (1996).
19. J. G. Khinast, D. Luss, *Comput. Chem. Eng.* **24**, 139 (2000).
20. S. Kádár, J. Wang, K. Showalter, *Nature* **391**, 770 (1998).
21. O. Steinbock, V. Zykov, S. C. Müller, *Nature* **366**, 322 (1993).
22. E. D. Sontag, *Mathematical Control Theory: Deterministic Finite-Dimensional Systems* (Springer-Verlag, Berlin, ed. 2, 1998).
23. E. Ott, C. Grebogi, J. A. Yorke, *Phys. Rev. Lett.* **64**, 1196 (1990).
24. V. S. Zykov, A. S. Mikhailov, S. C. Müller, *Phys. Rev. Lett.* **78**, 3398 (1997).
25. D. Semowogerere, M. F. Schatz, *Bull. Am. Phys. Soc.* **45**, 46 (2000).
26. R. Roy, K. S. Thornburg Jr., *Phys. Rev. Lett.* **72**, 2009 (1994).
27. V. K. Vanag, L. Yang, M. Dolnik, A. M. Zhabotinsky, I. R. Epstein, *Nature* **406**, 389 (2000).
28. Desired spatiotemporal heating patterns could be programmed into the control computer by using LabVIEW. In addition, it was possible to control the laser spot on the surface by hand directly, using the computer mouse. This joystick mode establishes—as in computer games or flight simulators—a direct feedback with the human brain as image processor and control action calculator. For our computer-controlled feedback experiments, real-time image processing and desired rules for the heating patterns and intensities were implemented in software.
29. O. Steinbock, J. Schütze, S. C. Müller, *Phys. Rev. Lett.* **68**, 248 (1992).
30. A. P. Munuzuri, M. Dolnik, A. M. Zhabotinsky, I. R. Epstein, *J. Am. Chem. Soc.* **121**, 8065 (1999).
31. In our experiments, the Pt(110) single-crystal sample was kept in an ultrahigh-vacuum apparatus. The surface was prepared by Ar-ion sputtering and annealing to about 1100 K. The quality of the surface preparation was checked with low-energy electron diffraction.
32. H. H. Rotermund, G. Haas, R. U. Franz, R. M. Tromp, G. Ertl, *Science* **270**, 608 (1995).
33. We have measured the spatiotemporal temperature profile of our laser spot using a cooled infrared (IR) camera with a temperature resolution of 0.05 K at room temperature. From those IR images we deduced a maximum differential temperature rise at the spot of about 15 K; typically, we worked at powers giving a temperature rise of 2 to 3 K over an area of ~80 μm in diameter. Detailed heat balance simulations, including radiation and conduction, showed that only 5 ms were needed to locally establish this differential temperature rise, confirming our experimental observation of a heat quench in less than 20 ms. In other words, the temperature rises and returns to its background state essentially instantaneously with the movement of the laser spot.
34. S. Völkening, J. Wintterlin, *J. Chem. Phys.* **114**, 6382 (2001).
35. D. Y. Kuan, H. T. Davis, R. Aris, *Chem. Eng. Sci.* **38**, 719 (1983).
36. G. J. Pappas, G. Lafferriere, S. Sastry, *IEEE Trans. Autom. Control* **45**, 1144 (2000).
37. M. D. Graham *et al.*, *Phys. Rev. E* **52**, 76 (1995).
38. We gratefully acknowledge partial support by the Office of Naval Research (I.G.K. and H.H.R.), NSF, Air Force Office of Scientific Research, and the Humboldt Foundation (I.G.K.), and by a Marie Curie Fellowship (A.G.P.) under contract HPMFCT-2000-00685. We thank M. Pollmann for the measurement of Fig. 1C and S. Shvartsman for many discussions.

19 June 2001; accepted 28 August 2001

Submicrometer Metallic Barcodes

Sheila R. Nicewarner-Peña,[1] R. Griffith Freeman,[2]
Brian D. Reiss,[1] Lin He,[2] David J. Peña,[1] Ian D. Walton,[2]
Remy Cromer,[2] Christine D. Keating,[1]* Michael J. Natan[2]*

We synthesized multimetal microrods intrinsically encoded with submicrometer stripes. Complex striping patterns are readily prepared by sequential electrochemical deposition of metal ions into templates with uniformly sized pores. The differential reflectivity of adjacent stripes enables identification of the striping patterns by conventional light microscopy. This readout mechanism does not interfere with the use of fluorescence for detection of analytes bound to particles by affinity capture, as demonstrated by DNA and protein bioassays.

Multiplexing and miniaturization are becoming pervasive themes in bioanalysis. The push to measure ever-increasing numbers of species from smaller and smaller sample volumes has led to innovative devices for sample manipulation [e.g., chip-based microfluidics (*1*)] and ingenious approaches to simultaneous measurement capabilities (e.g., mi-

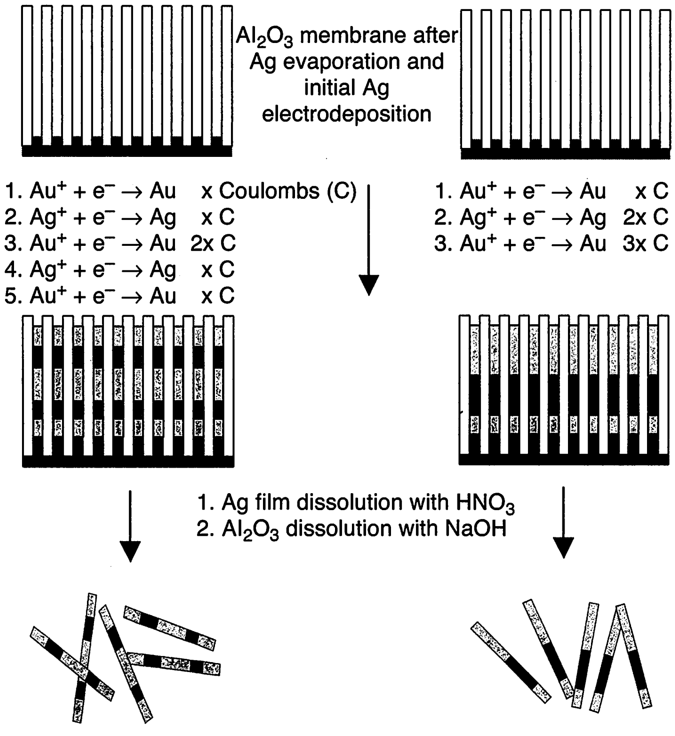

Fig. 1. Synthesis of barcoded particles.